Chemistry–A European Journal
Research Article
doi.org/10.1002/chem.202302527
Chemistry Europe
European Chemical Societies Publishing
www.chemeurj.org

Hot Paper

Structure and Flexibility of Copper-Modified DNA G-Quadruplexes Investigated by ^{19}F ENDOR Experiments at 34 GHz**

Simon L. Schumann,[a] Simon Kotnig,[a] Yury Kutin,*[a] Maria Drosou,[b] Lukas M. Stratmann,[a] Yana Streltsova,[a] Alexander Schnegg,[c] Dimitrios A. Pantazis,[b] Guido H. Clever,*[a] and Müge Kasanmascheff*[a]

DNA G-quadruplexes (GQs) are of great interest due to their involvement in crucial biological processes such as telomerase maintenance and gene expression. Furthermore, they are reported as catalytically active DNAzymes and building blocks in bio-nanotechnology. GQs exhibit remarkable structural diversity and conformational heterogeneity, necessitating precise and reliable tools to unravel their structure-function relationships. Here, we present insights into the structure and conformational flexibility of a unimolecular GQ with high spatial resolution via electron-nuclear double resonance (ENDOR) experiments combined with Cu(II) and fluorine labeling. These findings showcase the successful application of the ^{19}F-ENDOR methodology at 34 GHz, overcoming the limitations posed by the complexity and scarcity of higher-frequency spectrometers. Importantly, our approach retains both sensitivity and orientational resolution. This integrated study not only enhances our understanding of GQs but also expands the methodological toolbox for studying other macromolecules.

Introduction

Guanine-rich DNA sequences are able to form helical, four-stranded structures called G-quadruplexes (GQs), a class of DNA secondary motifs found in vivo and known to play essential roles in telomere maintenance, regulation of gene expression, and other biological processes.[1–5] GQs are further known to spontaneously form higher-order structures (dimers,[6–9] G-wires,[10,11] etc.), likely affecting their physiological function.[12–15] The regulatory function of GQs in various pathological processes makes them attractive drug targets, in particular in cancer research.[16–19] Additionally, GQs are explored as a structural motif in DNA-based catalysis[20–25] and nanotechnology.[26–28] All these topics and applications benefit from a precise understanding of the structures of involved GQs. Methods for DNA structure elucidation, however, are often complicated by hit-and-miss sample preparation (for single crystal X-ray diffraction) or tedious data interpretation (for unambiguous NMR structure elucidation).

Electron-nuclear double resonance (ENDOR) spectroscopy, combined with ^{19}F labeling, has been used to determine electron-nuclear distances for atomic-scale structure elucidation of various biopolymers.[29–32] This technique has been applied to ^{19}F-equipped biological macromolecules ranging from spin-labeled RNA to radical-containing protein machineries[33–37] in the last three years. However, all of these recent studies were carried out at the microwave (mw) frequency of 94 GHz (W-band) or higher, where the overlap with proton ENDOR resonances is avoided or minimized.[34,36] This simplifies the ^{19}F data analysis but limits access to the technique due to the scarcity and complexity of electron paramagnetic resonance (EPR) spectrometers operating at such high fields/high frequencies. Here, we overcome this shortcoming by extending ^{19}F ENDOR to a lower and more accessible mw frequency of 34 GHz (Q-band). Our findings provide insights into the structure and conformational flexibility of a modified DNA GQ and expand the toolbox for studying large biomolecules.

[a] S. L. Schumann, S. Kotnig, Dr. Y. Kutin, Dr. L. M. Stratmann, Y. Streltsova, Prof. Dr. G. H. Clever, Prof. Dr. M. Kasanmascheff
Department of Chemistry and Chemical Biology
TU Dortmund University
Otto-Hahn-Strasse 6, 44227 Dortmund (Germany)
E-mail: yury.kutin@tu-dortmund.de
guido.clever@tu-dortmund.de
muege.kasanmascheff@tu-dortmund.de
Homepage: https://ccb.tu-dortmund.de/en/professorships/pc/kasanmascheff
https://ccb.tu-dortmund.de/en/professorships/ac/clever

[b] Dr. M. Drosou, Dr. D. A. Pantazis
Max-Planck-Institut für Kohlenforschung
Kaiser-Wilhelm-Platz 1, 45470 Mülheim an der Ruhr (Germany)

[c] Dr. A. Schnegg
Max-Planck-Institut für Chemische Energiekonversion
Stiftstraße 34–36, 45470 Mülheim an der Ruhr (Germany)

[**] ENDOR = electron-nuclear double resonance.A previous version of this manuscript has been deposited on a preprint server (https://chemrxiv.org/engage/chemrxiv/article-details/646f32f3be16ad5c57e3626f).

Supporting information for this article is available on the WWW under https://doi.org/10.1002/chem.202302527

Results and Discussion

Cu(II)/^{19}F labeling and EPR characterization of GQs

Previously, we demonstrated that paramagnetic Cu(II) ions in square-planar tetrapyridine complexes can be covalently incorporated into tetramolecular GQs.[38,39] These complexes were utilized as highly rigid spin labels to precisely measure intra- and intermolecular Cu(II)–Cu(II) distances in GQs and higher-order GQ structures such as dimers and GQ-ligand adducts using pulsed dipolar EPR spectroscopy.[40,41] We also incorporated a Cu(pyridine)$_4$ complex into a unimolecular antiparallel GQ based on the 22-nucleobase human telomeric sequence (**GQ0**, Figure 1) by substituting a full guanine tetrad.[42] Several related modified structures have been reported as Cu(II)-dependent DNAzymes and aptamers.[23,42]

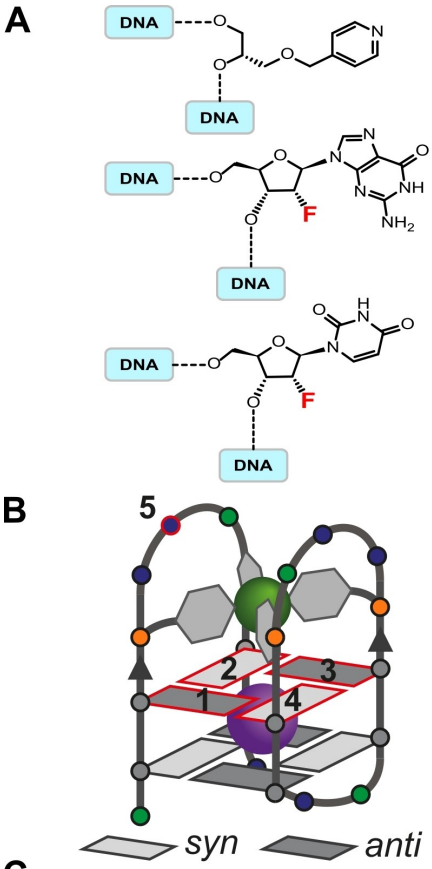

C

GQ species

0: 5′- AGG LTT ALG GTT AGG LTT ALG G - 3′
1: 5′- AG**G** LTT ALG GTT AGG LTT ALG G - 3′
2: 5′- AGG LTT AL**G** GTT AGG LTT ALG G - 3′
3: 5′- AGG LTT ALG GTT AG**G** LTT ALG G - 3′
4: 5′- AGG LTT ALG GTT AGG LTT AL**G** G - 3′
5: 5′- AGG LT**U** ALG GTT AGG LTT ALG G - 3′

Figure 1. (**A**) Incorporated modifications from top to bottom: pyridine ligand (L), 2′-fluoro-2′-deoxyguanosine (^{F}**G**), and 2′-fluoro-2′-deoxyuridine (^{F}**U**). (**B**) Schematic representation of the folded GQ structure modified with four pyridine-ligands (**GQ0**). One ^{19}F-containing ^{F}**G** was incorporated at one of the highlighted G positions in **GQ1**-**GQ4** (indicated by numbers 1–4). For **GQ5**, ^{F}**U** was introduced at position 5. Bound Cu(II) and K(I) cations are represented as a green and purple sphere, respectively. (**C**) GQ sequences used in this work. ^{19}F-modification sites are highlighted in red.

In the present study, we further modified the parental **GQ0** sequence by introducing a single ^{19}F-labeled guanosine residue (2′-fluoro-2′-deoxyguanosine, ^{F}**G**) at one of the four positions within the upper G-tetrad, resulting in four GQ species termed **GQ1**–**GQ4** (shown in Figure 1, see Supporting Information 1.1–1.6 for details). Additionally, we synthesized species **GQ5** by replacing a thymidine with a ^{19}F-labeled uridine (2′-fluoro-2′-deoxyuridine, ^{F}**U**) in the loop region close to the Cu(II) binding site. Prior to EPR measurements, we characterized these samples via CD and UV-based thermal denaturation experiments. The former demonstrated that **GQ1**–**GQ5** adopted the same overall structure as the ^{19}F-free species **GQ0** (see Supporting Information 1.5), while the latter revealed significantly lower melting temperatures for **GQ2** and **GQ4** (approximately 20 °C below that of **GQ0**, see Supporting Information 1.4). The destabilizing effect of the 2′-fluorinated residues on GQs due to electrostatic repulsion between phosphate and the 2′-fluorine has been previously reported.[43–45] The modification of guanosines in the *syn*-conformation tends to result in a stronger destabilization than that of the *anti*-conformers, in line with the reduction of the melting temperatures for **GQ2**/**GQ4**, but not for **GQ1**/**GQ3** (see Table S1). To minimize unfolding of the quadruplexes during the sample preparation, **GQ2**/**GQ4** were transferred into EPR tubes at an ambient temperature of 4 °C (see Supporting Information 2.3 and Figure S2).

A comparison of echo-detected Q-band EPR spectra of **GQ1**-**GQ5** revealed almost identical line shapes, with **GQ2** and **GQ4** showing marginal distortions. The spectra are dominated by typical axial *g*- and copper hyperfine (hf) tensors, consistent with our previously reported Cu(II)-labeled GQ structures.[38,40,41] Overall, these findings demonstrate that the effects of ^{19}F-labeling on the Cu(II) electronic structure are negligible. A representative spectrum can be found in Figure 2A, and additional spectra are shown in Figures S1–S2.

^{19}F tag orientations and Cu(II)—^{19}F ENDOR. As all prepared ^{19}F-labeled GQs exhibited the same structure as **GQ0**, we built upon the previously published molecular dynamics (MD) simulation data of **GQ0**.[42] We anticipated two distinct Cu(II)—^{19}F distances and ^{19}F angular positions with respect to the Cu(II) *g*-tensor orientation. For **GQ1**/**GQ3**, the F atom was expected to point towards the Cu(II) label, whereas for **GQ2**/**GQ4**, it was expected to point away from it, referred to as 'up' and 'down' orientations (see Figure 2B and Supporting Information 1.6). The Cu(II)—^{19}F distances upon labeling in all cases were anticipated on the order of 1 nm (SI3), resulting in ^{19}F ENDOR splittings of approximately 0.1 MHz (see Equation S4). Therefore, we employed Mims ENDOR,[46] which is highly sensitive to such small hf couplings but requires careful optimization of the mw pulse separation times (see Supporting Information 2.4 for details).

Spectral analysis at Q-band was complicated by the small separation between the ^{19}F and ^{1}H Larmor frequencies (~3 MHz), which resulted in overlapping spectral features. However, clean ^{19}F Mims ENDOR spectra were obtained by subtracting the ^{1}H background using the non-labeled sequence

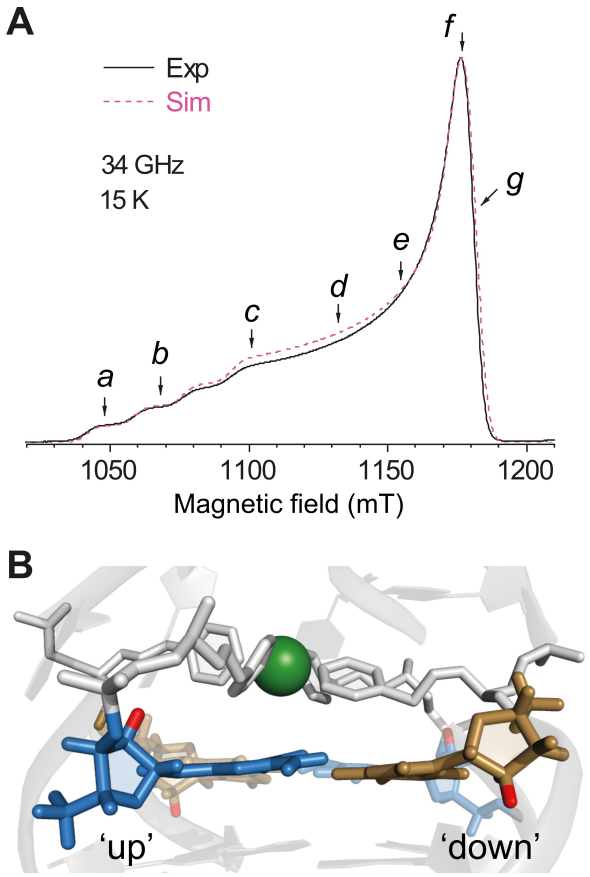

Figure 2. (**A**) A representative echo-detected EPR spectrum for a sample carrying the ^{19}F tag at position 3 (**GQ3**) recorded at 34 GHz (black solid trace) with the corresponding simulation (pink dashed trace). Simulation parameters: $g_\perp = 2.061$, $g_\parallel = 2.275$, $A_\parallel = 555$ MHz (see Supporting Information 2.1-2.3 for details of the experimental conditions and simulations). Field positions where ENDOR spectra were measured are marked *a* to *g*. (**B**) The 'up' and 'down' conformations are shown with blue and gold sticks, respectively. The protons exchanged for ^{19}F in this study are shown in red.

GQ0, as shown in Figures 3, S5, and S6 (see details of the background subtraction in Supporting Information 2.5). To detect the full hf tensor, we recorded several orientation-selective Mims ENDOR spectra over the entire EPR envelope. The chosen field positions are marked with *a*-*g* in Figure 2A, and the corresponding excited *g*-tensor orientations are given in Figure S7. Note that the ENDOR line shapes of the GQs within each pair of species (**GQ1**/**GQ3** and **GQ2**/**GQ4**) are almost identical, demonstrating that the spin-labeled GQs form well-defined and symmetric structures (see Figure S8). In contrast, the ENDOR patterns of the 'up' and 'down' orientations are clearly distinct, as expected. For example, the broadest ENDOR features of **GQ1**/**GQ3** and **GQ2**/**GQ4** are observed in traces *g* and *c*-*d*, respectively (Figure 3A vs. 3E).

The major differences between **GQ1**/**GQ3** and **GQ2**/**GQ4** ENDOR patterns can be rationalized based on the nuclear position coordinate β with respect to the Cu(II) *g*-tensor (see Figure 3B for **GQ1**/**GQ3** and S9 for **GQ2**/**GQ4**). This coordinate affects the angle θ between the static magnetic field ($\boldsymbol{B}_0$) and the inter-spin vector excited at each observer field (labeled *a*-*g*), which, in turn, determines the frequencies of ENDOR transitions.[47,48] At the field position *a* ($\boldsymbol{B}_0 \parallel g_z$, or $g_\parallel$), a single inter-spin vector orientation (θ_z, Figure 3C) is excited, resulting in a narrow ENDOR signal. In contrast, at position *g*, where $\boldsymbol{B}_0$ is in the $g_\perp$ (g_x, g_y) plane, a broad range of orientations are excited for **GQ1**/**GQ3** (from θ_x to θ_y, Figure 3D), producing a broad ENDOR feature with two maxima. With this understanding, all ENDOR traces were well-reproduced in the spectral simulations (dashed red traces in Figures 3A and S6, see Table 1 and Supporting Information 2.8 for details).

Minimization of the root-mean-square deviation (RMSD) between the simulated and experimental ENDOR traces yielded precise values for the Cu(II)–^{19}F inter-spin distance (*d*) and the orientation of the inter-spin vector with respect to the g_z axis (β). The isotropic hf term (A_{iso}) was found to be approximately zero for all labeling positions. RMSD heatmaps for the ENDOR simulations of **GQ1** are given in Figure 4. Each heatmap was plotted for a pair of fitting parameters, with the third parameter set to its optimized value. All optimized parameters are listed in Table 1, which demonstrates that not only distances but also relative orientations of ^{19}F with respect to Cu(II) can be determined precisely (more information on the simulations can be found in Supporting Information 2.10 and 2.11). The determined β angles were in agreement with the expected values for the 'up' and 'down' conformations (Figure 2B and Supporting Information 1.6).

Computational investigation

To relate the experimental data to computationally derived models, we performed MD simulations on **GQ1** and **GQ3**, and selected structural snapshots that matched the Cu(II)–^{19}F distances *d* and exhibited high symmetry. Using these structural models, we calculated ^{19}F hf couplings via density functional theory (DFT). DFT calculations on MD snapshots for **GQ1** and **GQ3** ($d_1 = 8.359$ Å and $d_2 = 8.391$ Å, respectively) reproduced the hf coupling tensor determined via ^{19}F ENDOR, confirming the consistency of the point dipole approximation for this system (see Table S4). Additionally, the computed *g*-tensors agreed with the experimental values, indicating that the spin density distribution was accurately described by DFT.[49] Further details on the MD and DFT investigations can be found in the Supporting Information (SI3–4).

Table 1. The isotropic hf term (A_{iso}), ^{19}F angular position (β), and distance between Cu(II) and ^{19}F (*d*) obtained from the orientation-selective ENDOR simulations for the GQ species **GQ1**–**GQ4**. The experimental uncertainties were estimated as ranges where the RMSD reaches 115% of its minimal value (see S2.11).

Sample	$A_{iso,\,sim}$/kHz	β_{sim}/deg	d_{sim}/Å
GQ1	−1 ± 6	98 ± 5	8.2 ± 0.1
GQ3	−1 ± 6	100 ± 4	8.3 ± 0.1
GQ2	0 ± 8	131 ± 7	10.7 ± 0.4
GQ4	2 ± 10	131 ± 10	10.5 ± 0.5

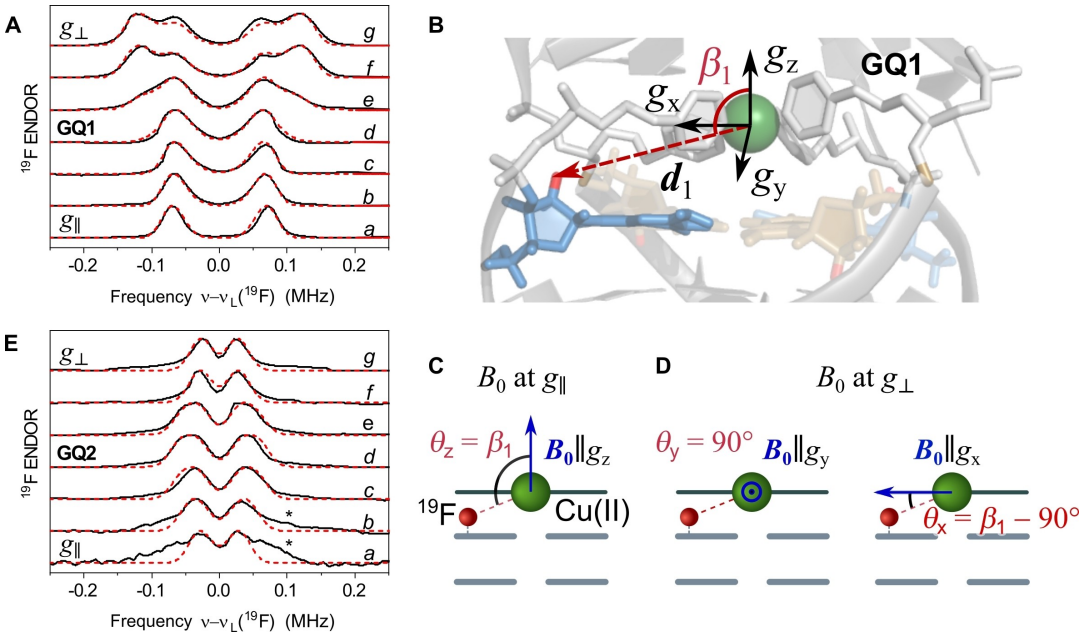

Figure 3. (**A**,**E**) Normalized orientation-selective ^{19}F Mims ENDOR spectra of **GQ1** and **GQ2** in deuterated buffer recorded at 15 K at several field positions marked in Figure 2A (black traces), overlaid with spectral simulations (red dashed traces). Each spectrum was normalized to its maximum intensity; optimized τ values for each field position are given in Table S2. Asterisks mark broad spectral features originating from the denatured GQ fraction. (**B**) Inter-spin vector ***d*** and angular position β for the ^{19}F tag in **GQ1** with respect to the Cu(II) *g*-tensor (***d***$_1$ and β_1 refer to the parameters observed in **GQ1**). (**C**,**D**) Angle θ between ***d*** and $\boldsymbol{B}_0$ for the three orientations of the magnetic field along the canonical directions of the Cu(II) *g*-tensor. See Supporting Information 2.8 for **GQ2**, characterized by a larger angle $\beta_2 > \beta_1$.

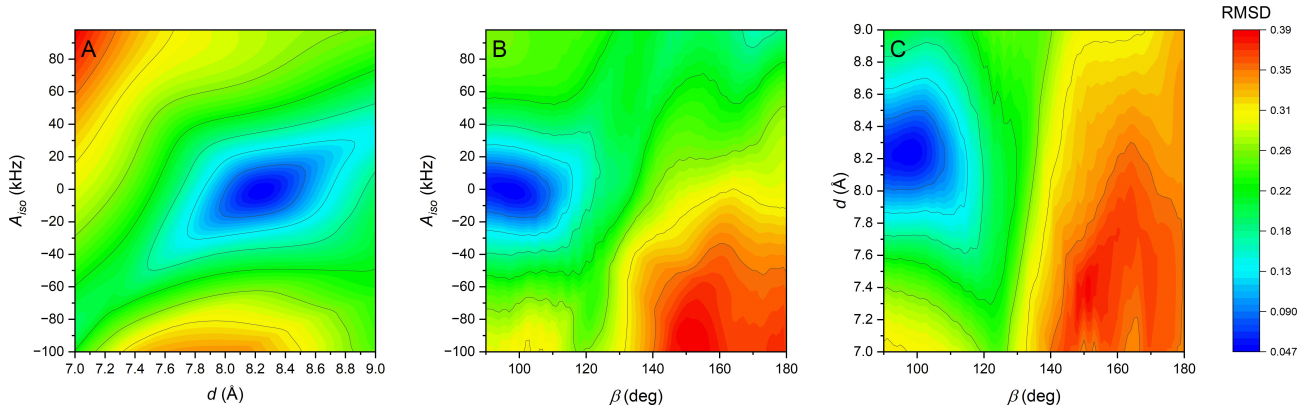

Figure 4. RMSD heatmap plots for the ^{19}F angular position (β), inter-spin Cu(II)–^{19}F distance (*d*), and the isotropic hf term (A_{iso}), used to fit the orientation-selective ENDOR data of **GQ1** (Figure 3A and S6). Each heatmap is plotted for a pair of fitting parameters, with the third parameter set to its optimized value (Table 1).

^{19}F labeling of the loop region

In this study, we not only investigated the rigid G-tetrad region of GQs using **GQ1**-**GQ4**, but we also tested the feasibility of using our Q-band ^{19}F ENDOR approach to explore the dynamic regions of GQs. We did this by studying species **GQ5**, with the ^{19}F tag incorporated in the loop region, which is expected to have some flexibility due to the absence of hydrogen bonding networks. As predicted, the conformational heterogeneity of **GQ5** resulted in broad and poorly resolved ^{19}F ENDOR spectra (Figure 5). We note that we also observed broad ^{19}F spectral features with partially unfolded **GQ2**/**GQ4** samples (Figure S11). However, unlike these samples, ^{19}F labeling in **GQ5** did not cause a destabilization of the GQ structure (see Supporting Information 1.4 and Figure S2). Therefore, the broad ENDOR features observed for **GQ5** demonstrate the flexibility of the loop region. These findings show the capability of ^{19}F ENDOR at Q-band to identify dynamic regions within folded DNA structures.

Comparison of Q- and W-band ENDOR

Finally, we analyzed the advantages and disadvantages of our approach for the investigated systems by comparing the ^{19}F ENDOR results at Q- and W-band. For a direct comparison, we

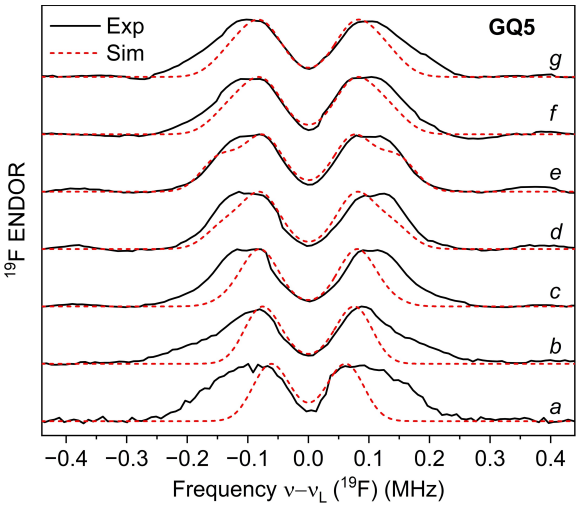

Figure 5. Normalized orientation-selective ^{19}F Mims ENDOR spectra of **GQ5** in deuterated buffer recorded at 15 K at several field positions marked in Figure 2A (black traces), overlaid with spectral simulations (red dashed traces) for $d = 7.8$ Å, $\beta = 65°$. The flexibility of the loop region leads to multiple ^{19}F tag conformations with a significant and anisotropic ENDOR line broadening, producing uncertainty in the simulations (see Supporting Information 2.11 and Figures S13–S14).

collected W-band ENDOR data for **GQ3** at the field positions corresponding to approximately the same effective *g*-values as at Q-band (positions *b*-*g*, see Figures 6, S15, and Supporting Information 2.12). Overlaying ^{19}F ENDOR spectra at both frequencies revealed almost identical line shapes (Figure S15), which could be attributed to the significant *g*-anisotropy that is already well-resolved at Q-band. The W-band spectra did not provide additional structural information and could be simulated using the ^{19}F hf tensor determined at Q-band (Figure 6).

Notably, the ENDOR line width, which sets the upper limit of the accessible distance range, remained almost unchanged between Q- and W-bands in our study (FWHM ≈ 36 kHz for **GQ3** at $g_{||}$). Furthermore, we assessed the influence of background

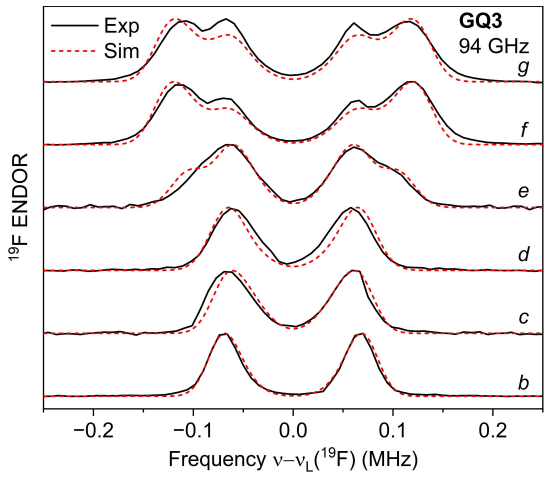

Figure 6. Normalized orientation-selective ^{19}F Mims ENDOR spectra of **GQ3** in deuterated buffer recorded at 94 GHz (black traces), overlaid with spectral simulations (red dashed traces). Simulations employed the ^{19}F hf tensor obtained from the 34 GHz dataset without additional optimization.

subtraction on the data quality and found that the ^{19}F ENDOR data at both frequencies showed similar signal-to-noise ratios normalized to the acquisition time (see Supporting Information 2.13 and Table S3).

Conclusions

Our study demonstrates that the precise determination of key structural features of DNA GQs at atomic-scale resolution in frozen aqueous solutions can be achieved through ENDOR spectroscopy at Q-band combined with Cu(II) and ^{19}F labeling. Our four-point-fixed, rigid Cu(II) spin label was designed for DNA GQs and allowed distance measurements in the approximate range of 8–11 Å with a high accuracy of up to 0.1 Å, depending on the distance and labeling site. This approach also distinguished a flexible structural moiety within the folded DNA GQ motif from a rigid one, which is crucial for understanding the structure of novel GQs.

Our future plans include applying the methodology to characterize the substrate docking to the Cu(II) catalytic site of GQ-based metalloDNAzymes, shown to catalyze the Michael addition reaction with excellent yields and enantioselectivity.[23] In such a system, the GQ is modified with copper, while the ^{19}F tag is incorporated into the substrate. Conversely, binding modes of GQs with Cu(II)-containing ligands such as porphyrins[50] can be studied with the GQ carrying only the minimal ^{19}F modification. Additionally, our method can help identify the sites and modes of GQ-protein interactions[51] via changes in the loop flexibility upon protein binding. Thus, our findings expand the toolbox of structure elucidation methods for macromolecules, providing new opportunities for broader applications of ENDOR-based distance measurements.

The technique shows promise for the diverse group of copper-containing proteins, for example, particulate methane monooxygenase,[52] as well as Cu(II)-based spin labels such as Cu(II)–DPA[53,54] and Cu(II)-binding dHis motif[55–57] utilized for pulsed dipolar EPR studies of nucleic acids and proteins, respectively. Additionally, the method is not limited to Cu(II)-based spin probes. Other paramagnetic centers with a significant *g*-anisotropy, such as FeS clusters and heme centers, are expected to be resolved at Q-band without the loss of orientational information.

Finally, the latest developments in Q-band EPR instrumentation concerning the cryogenic signal preamplification[58] reducing the acquisition time by a factor of ~40 in certain cases, further boost the relevance and future potential of the Q-band ^{19}F ENDOR implementation over W-band. We anticipate this method to be widely utilized in DNA research to investigate the structural diversity and flexibility of GQs, further oligonucleotide motifs, DNA-protein complexes, and metalloDNAzymes.

Experimental Section

Synthesis and Purification: The synthesis of the pyridine building block L was carried out as described in the literature.[42] Only the

(*S*)-enantiomer was used in this study. All oligonucleotides were synthesized on a *K&A Laborgeraete GbR H-8* synthesizer on a 1 μmol scale using the standard phosphoramidite methods on CPG and following previously published procedures for synthesis.[39,42] Standard phosphoramidites (DMT-dT-CEP, DMT-dA(bz)-CEP and DMT-dG(*i*Bu)-CEP) as well as modified phosphoramidites (DMT-2′-fluoro-dU-CEP and DMT-2′-fluoro-dG(*i*b)-CEP) were used. Purification of the oligonucleotides was performed as described in literature,[41] with reversed-phase HPLC on an *Agilent Technologies 1260 Infinity II* HPLC system equipped with an autosampler, column oven, DAD detector and a *Macherey-Nagel VP 250/10 NUCLEODUR 100-5C18ec* column (oven temperature: 60 °C, flow rate: 2.5 mL/min, solvent A: 50 mM TEAA pH 7, solvent B: 70 : 30 MeCN/50 mM TEAA pH 7, gradient: from 100 % solvent A to 20 % solvent A and 80 % solvent B in 30 min). Collected product fractions were lyophilized overnight using a *Christ Alpha 2–4 LSCBasic* lyophilisation device and then dissolved in 1–2 mL of 100 mM TEAA buffer pH = 7.0. Subsequently, the cleavage of the 5′-OH DMT protecting groups (with 2 % TFA) and desalting were accomplished using *Waters Sep-Pak C18* cartridges.

Analytics of Oligonucleotides: To check the oligonucleotide purity, samples (10 μL) with DNA concentrations of around 500 μM in 20 mM TEAA pH 7 were prepared, and analytical RP-HPLC was performed on an *Agilent Technologies 1260 Infinity II system* equipped with an autosampler, column oven, DAD detector and a *Macherey-Nagel EC 250/4.6 NUCLEODUR 100–5 C18ec* column (oven temperature: 60 °C, flow rate: 0.75 mL/min, solvent A: 50 mM TEAA pH 7, solvent B: 70 : 30 MeCN/50 mM TEAA pH 7).

UV-Vis and CD characterization of G-Quadruplexes: All measured samples contained 4 μM DNA, 4 μM $CuSO_4$, 100 mM KCl, and 10 mM lithium cacodylate buffer pH 7.2. For all experiments, samples were prepared with ultrapure water (type I, 18.2 MΩ cm), obtained with a *VWR Puranity TU 3 UV* device. Samples were heated at 85 °C for 10 min, slowly cooled to 4 °C with a cooling rate of 0.5 °C/min, and then left at this temperature for several hours (typically overnight).

The *Jasco V-650 UV-Visible Spectrophotometer* equipped with a *PAC-743 6-cell thermostat* for temperature control was used to measure the melting curves and TDS spectra. Quartz glass cuvettes *(Hellma Analytics114-QS*, 1 cm path length) were used for the measurements. For the melting curves, absorbance at the wavelength of 295 nm was plotted, with the signal at 350 nm used for background correction. The data points were recorded from 0 °C to 85 °C, with the temperature increasing by 0.5 °C/min. The melting temperature was determined by finding the inflection point of the melting curve. For the thermal difference spectra (TDS), a UV-Vis spectrum was recorded between 220 and 350 nm at 0 °C (folded condition) and 85 °C (unfolded condition). The absorbance values at 350 nm were used for background correction. Subsequently, the measured data of the folded GQs were subtracted from the measured data of the unfolded GQs.

CD spectra were measured on an *Applied Photophysics Chirascan qCD spectropolarimeter* (350–220 nm, 0.5 s time-per-point, step size 1 nm, bandwidth 0.5 nm, 3 repeats) at 4–7 °C. The temperature was controlled using a *Quantum Northwest* temperature control attached to a sample probe. All spectra were averaged, background-corrected (cuvette, buffer, and electrolyte), smoothed (Savitzky-Golay, window size 5), and zeroed to the signal at 350 nm.

EPR/ENDOR Spectroscopy: All starting sample solutions contained 2 mM DNA, 2 mM $CuSO_4$, and 50 mM potassium phosphate buffer pH 7, and were prepared with ultrapure water (type I, 18.2 MΩ cm). The water was then removed by lyophilization, and the solid was then dissolved in D_2O. For GQ folding, the solution was heated at 85 °C for 10 min, slowly cooled to 4 °C with a cooling rate of 0.5 °C/min, and then left at this temperature for several hours (typically overnight). After completion of the GQ folding, the DNA solution was placed on ice and mixed 1 : 1 (v/v) with glycerol-d8, which had also been stored on ice. Sample solutions (**GQ0**–**GQ5**) containing the final DNA concentration of 1 mM (~20 μL) were transferred into 1.6 OD ilmasil® PN quartz tubes, flash-frozen in liquid nitrogen, and stored at approximately −196 °C.

34 GHz (Q-band) EPR and ENDOR measurements were carried out at 15 K using a Bruker Elexsys E580 spectrometer equipped with a 150 W TWT amplifier (Applied System Engineering, 187Ka), commercial Bruker EN 5107D2 ENDOR resonator, Oxford Instruments CF935 continuous-flow helium cryostat and Oxford Instruments MercuryiTC temperature controller. ENDOR experiments were performed using an AR 600 W radiofrequency (RF) amplifier (AR 600 A225 A) with the standard Mims ENDOR sequence[46] with a 45 μs RF pulse. The inter-pulse delay τ was optimized for each measurement, as described in the Supporting Information. ^{1}H Davies ENDOR spectra were collected using the same equipment, following the standard Davies[59] sequence with a 17 μs RF pulse and a 200 ns inversion pulse. 94 GHz (W-band) EPR and ENDOR measurements were carried out at approximately 4.4 K (except for the ENDOR trace *g* in Figure 6 and the trace in Figure S17, which were collected at 15 K) using a Bruker Elexsys E680 spectrometer equipped with a 2 W mw amplifier (Quinstar, model QPP-94013338MPI), commercial Bruker EN 680-1021H ENDOR resonator and a closed-cycle 6 T Cryogenic J4233 split-pair superconducting magnet with an integrated 2–300 K cryostat. Mims ENDOR experiments were carried out using a 100 W RF amplifier (Mini-Circuits ZHL-100 W-GAN+). EPR and ENDOR simulations were performed using the *EasySpin* package (versions 6.0.0-dev.36-51).[60]

For details, see the corresponding Materials and Methods sections in the Supporting Information.

Supporting Information

The authors have cited additional references within the Supporting Information.[61–94]

Acknowledgements

We thank Dr. Leonid Rapatskiy for his assistance with the W-band measurements, Victor Selve for supporting the Matlab coding, and Thorsten Bürger for his help with some of the Mims ENDOR measurements. MD, AS and DAP acknowledge support by the Max Planck Society and MD acknowledges support from the Alexander von Humboldt Foundation. This work is funded by the Deutsche Forschungsgemeinschaft (DFG, German Research Foundation) under Germany's Excellence Strategy – EXC 2033-390677874-RESOLV, and via the grants CL489/4-1 and KA4774/3-1. Open Access funding enabled and organized by Projekt DEAL.

Conflict of Interests

The authors declare no conflict of interest.

Data Availability Statement

The data that support the findings of this study are available from the corresponding author upon reasonable request.

Keywords: DNA · ENDOR spectroscopy · EPR spectroscopy · ^{19}F labeling · G-quadruplexes

[1] D. Rhodes, H. J. Lipps, *Nucleic Acids Res.* **2015**, *43*, 8627–8637.
[2] M. L. Bochman, K. Paeschke, V. A. Zakian, *Nat. Rev. Genet.* **2012**, *13*, 770–780.
[3] R. Hänsel-Hertsch, M. D. Antonio, S. Balasubramanian, *Nat. Rev. Mol. Cell Biol.* **2017**, *18*, 279–284.
[4] T. Tian, Y.-Q. Chen, S.-R. Wang, X. Zhou, *Chem* **2018**, *4*, 1314–1344.
[5] S. Chaudhary, M. Kumar, M. Kaushik, *Int. J. Biol. Macromol.* **2022**, *219*, 414–427.
[6] D. Sen, W. Gilbert, *Biochemistry* **1992**, *31*, 65–70.
[7] Y. Wang, D. J. Patel, *Biochemistry* **1992**, *31*, 8112–8119.
[8] Y. Krishnan-Ghosh, D. Liu, S. Balasubramanian, *J. Am. Chem. Soc.* **2004**, *126*, 11009–11016.
[9] Y. Kato, T. Ohyama, H. Mita, Y. Yamamoto, *J. Am. Chem. Soc.* **2005**, *127*, 9980–9981.
[10] T. C. Marsh, E. Henderson, *Biochemistry* **1994**, *33*, 10718–10724.
[11] K. Bose, C. J. Lech, B. Heddi, A. T. Phan, *Nat. Commun.* **2018**, *9*, 1959–1959.
[12] V. Kuryavyi, A. T. Phan, D. J. Patel, *Nucleic Acids Res.* **2010**, *38*, 6757–6773.
[13] V. T. Mukundan, N. Q. Do, A. T. Phan, *Nucleic Acids Res.* **2011**, *39*, 8984–8991.
[14] M. Adrian, D. J. Ang, C. J. Lech, B. Heddi, A. Nicolas, A. T. Phan, *J. Am. Chem. Soc.* **2014**, *136*, 6297–6305.
[15] S. Kolesnikova, E. A. Curtis, *Molecules* **2019**, *24*, 3074–3074.
[16] L. Oganesian, T. M. Bryan, *BioEssays* **2007**, *29*, 155–165.
[17] S. Neidle, *FEBS J.* **2010**, *277*, 1118–1125.
[18] N. S. Ilyinsky, A. M. Varizhuk, A. D. Beniaminov, M. A. Puzanov, A. K. Shchyolkina, D. N. Kaluzhny, *Mol. Biol.* **2014**, *48*, 778–794.
[19] A. Veselov, R. M. Burger, C. P. Scholes, *J. Am. Chem. Soc.* **1998**, *120*, 1030–1033.
[20] J. Dong, M. P. O'Hagan, I. Willner, *Chem. Soc. Rev.* **2022**, *51*, 7631–7661.
[21] J. H. Yum, S. Park, H. Sugiyama, *Org. Biomol. Chem.* **2019**, *17*, 9547–9561.
[22] P. M. Punt, G. H. Clever, *Chem. Sci.* **2019**, *10*, 2513–2518.
[23] P. M. Punt, M. D. Langenberg, O. Altan, G. H. Clever, *J. Am. Chem. Soc.* **2021**, *143*, 3555–3561.
[24] S. Dey, A. Jäschke, *Angew. Chem. Int. Ed.* **2015**, *54*, 11279–11282.
[25] S. Roe, D. J. Ritson, T. Garner, M. Searle, J. E. Moses, *Chem. Commun.* **2010**, *46*, 4309–4311.
[26] S. Yang, W. Liu, R. Nixon, R. Wang, *Nanoscale* **2018**, *10*, 3626–3630.
[27] J. Wang, Z. Zhou, Z. Li, I. Willner, *Chem. Sci.* **2021**, *12*, 341–351.
[28] Y. Yu, Y. Zhou, M. Zhu, M. Liu, H. Zhu, Y. Chen, G. Su, W. Chen, H. Peng, *Chem. Commun.* **2019**, *55*, 5131–5134.
[29] G. B. Wells, M. W. Makinen, *J. Am. Chem. Soc.* **1988**, *110*, 6343–6352.
[30] F. Jiang, S.-W. Tsai, S. Chen, M. Makinen, *J. Phys. Chem. B* **1998**, *102*, 4619–4627.
[31] D. Lukoyanov, R. M. Burger, C. P. Scholes, *J. Am. Chem. Soc.* **2001**, *123*, 12742–12743.
[32] A. Kehl, M. Hiller, F. Hecker, I. Tkach, S. Dechert, M. Bennati, A. Meyer, *J. Magn. Reson.* **2021**, *333*, 107091.
[33] N. B. Asanbaeva, A. A. Sukhanov, A. A. Diveikina, O. Y. Rogozhnikova, D. V. Trukhin, V. M. Tormyshev, A. S. Chubarov, A. G. Maryasov, A. M. Genaev, A. V. Shernyukov, G. E. Salnikov, A. A. Lomzov, D. V. Pyshnyi, E. G. Bagryanskaya, *Phys. Chem. Chem. Phys.* **2022**, *24*, 5982–6001.
[34] A. Meyer, S. Dechert, S. Dey, C. Höbartner, M. Bennati, *Angew. Chem. Int. Ed.* **2020**, *59*, 373–379.
[35] M. Judd, E. H. Abdelkader, M. Qi, J. R. Harmer, T. Huber, A. Godt, A. Savitsky, G. Otting, N. Cox, *Phys. Chem. Chem. Phys.* **2022**, *24*, 25214–25226.
[36] A. Meyer, A. Kehl, C. Cui, F. A. K. Reichardt, F. Hecker, L.-M. Funk, M. K. Ghosh, K.-T. Pan, H. Urlaub, K. Tittmann, J. Stubbe, M. Bennati, *J. Am. Chem. Soc.* **2022**, *144*, 11270–11282.
[37] M. Seal, W. Zhu, A. Dalaloyan, A. Feintuch, A. Bogdanov, V. Frydman, X.-C. Su, A. M. Gronenborn, D. Goldfarb, *Angew. Chem. Int. Ed.* **2023**, *62*, e202218780.
[38] D. M. Engelhard, R. Pievo, G. H. Clever, *Angew. Chem. Int. Ed.* **2013**, *52*, 12843–12847.
[39] D. M. Engelhard, L. M. Stratmann, G. H. Clever, *Chem. Eur. J.* **2018**, *24*, 2117–2125.
[40] D. M. Engelhard, A. Meyer, A. Berndhäuser, O. Schiemann, G. H. Clever, *Chem. Commun.* **2018**, *54*, 7455–7458.
[41] L. M. Stratmann, Y. Kutin, M. Kasanmascheff, G. H. Clever, *Angew. Chem. Int. Ed.* **2021**, *60*, 4939–4947.
[42] D. M. Engelhard, J. Nowack, G. H. Clever, *Angew. Chem. Int. Ed.* **2017**, *56*, 11640–11644.
[43] N. Martín-Pintado, M. Yahyaee-Anzahaee, G. F. Deleavey, G. Portella, M. Orozco, M. J. Damha, C. González, *J. Am. Chem. Soc.* **2013**, *135*, 5344–5347.
[44] Z. Li, C. J. Lech, A. T. Phan, *Nucleic Acids Res.* **2014**, *42*, 4068–4079.
[45] J. Dickerhoff, L. Haase, W. Langel, K. Weisz, *ACS Chem. Biol.* **2017**, *12*, 1308–1315.
[46] W. B. Mims, *Proc. R. Soc. London Ser. A* **1965**, *283*, 452–457.
[47] G. G. Hurst, T. A. Henderson, R. W. Kreilick, *J. Am. Chem. Soc.* **1985**, *107*, 7294–7299.
[48] T. A. Henderson, G. C. Hurst, R. W. Kreilick, *J. Am. Chem. Soc.* **1985**, *107*, 7299–7303.
[49] M. Drosou, C. A. Mitsopoulou, M. Orio, D. A. Pantazis, *Magnetochemistry* **2022**, *8*, 36.
[50] M. P. Donohue, V. A. Szalai, *Phys. Chem. Chem. Phys.* **2022**, *18*, 15447–15455.
[51] V. Meier-Stephenson, *Biophys. Rev. Lett.* **2022**, *14*, 635–654.
[52] M. O. Ross, F. MacMillan, J. Wang, A. Nisthal, T. J. Lawton, B. D. Olafson, S. L. Mayo, A. C. Rosenzweig, B. M. Hoffman, *Science* **2019**, *364*, 566–570.
[53] J. Casto, A. Mandato, L. Hofmann, I. Yakobov, S. Ghosh, S. Ruthstein, S. Saxena, *Chem. Sci.* **2022**, *13*, 1693–1697.
[54] S. Ghosh, M. J. Lawless, H. J. Brubaker, K. Singewald, M. R. Kurpiewski, L. Jen-Jacobson, S. Saxena, *Nucleic Acids Res.* **2020**, *48*, e49–e49.
[55] A. G. Jarvi, K. Ranguelova, S. Ghosh, R. T. Weber, S. Saxena, *J. Phys. Chem. B* **2018**, *122*, 10669–10677.
[56] M. J. Lawless, J. R. Pettersson, G. S. Rule, F. Lanni, S. Saxena, *Biophys. J.* **2018**, *114*, 592–601.
[57] J. L. Wort, K. Ackermann, A. Giannoulis, A. J. Stewart, D. G. Norman, B. E. Bode, *Angew. Chem. Int. Ed.* **2019**, *58*, 11681–11685.
[58] V. Kalendra, J. Turcak, G. Usevicius, H. Karas, M. Hülsmann, A. Godt, G. Jeschke, J. Banys, J. J. L. Morton, M. Simenas, *ChemRxiv preprint* **2023**, DOI: 10.26434/chemrxiv-2023-mghr2.
[59] E. R. Davies, *Phys. Lett. A* **1974**, *47*, 1–2.
[60] S. Stoll, A. Schweiger, *J. Magn. Reson.* **2006**, *178*, 42–55.
[61] M. J. Cavaluzzi, P. N. Borer, *Nucleic Acids Res.* **2004**, *32*, e13.
[62] J. Dickerhoff, K. Weisz, *J. Phys. Chem. Lett.* **2017**, *8*, 5148–5152.
[63] J. Dickerhoff, K. Weisz, *Angew. Chem. Int. Ed.* **2015**, *54*, 5588–5591.
[64] W. Bruggemann, J. R. Niklas, *J. Magn. Reson. Ser. A* **1994**, *108*, 25–29.
[65] J. S. Hyde, M. Pasenkiewicz-Gierula, A. Jesmanowicz, W. E. Antholine, *Appl. Magn. Reson.* **1990**, *1*, 483.
[66] C. Gemperle, A. Schweiger, *Chem. Rev.* **1991**, *91*, 1481–1505.
[67] J. R. Harmer, *eMagRes*, Vol.5 (Eds.: R. K. Harris, R. L. Wasylishen), John Wiley & Sons, Ltd, Chichester **2016**, 1493–1514.
[68] A. Collauto, V. Frydman, M. D. Lee, E. H. Abdelkader, A. Feintuch, J. D. Swarbrick, B. Graham, G. Otting, D. Goldfarb, *Phys. Chem. Chem. Phys.* **2016**, *18*, 19037–19049.
[69] F. D. Breitgoff, K. Keller, M. Qi, D. Klose, M. Yulikov, A. Godt, G. Jeschke, *J. Magn. Reson.* **2019**, *308*, 106560.
[70] G. R. Eaton, S. S. Eaton, *Multifrequency Electron Paramagnetic Resonance: Theory and Applications* (Ed.: S. K. Misra), Wiley-VCH Verlag GmbH & Co. KGaA, Weinheim **2011**, pp. 719–753.
[71] S. Pronk, S. Páll, R. Schulz, P. Larsson, P. Bjelkmar, R. Apostolov, M. R. Shirts, J. C. Smith, P. M. Kasson, D. van der Spoel, B. Hess, E. Lindahl, *Bioinformatics* **2013**, *29*, 845–854.
[72] D. van der Spoel, E. Lindahl, B. Hess, G. Groenhof, A. E. Mark, H. J. C. Berendsen, *J. Comput. Chem.* **2005**, *26*, 1701–1718.
[73] C. E. Jackson, C.-Y. Lin, J. van Tol, J. M. Zadrozny, *Chem. Phys. Lett.* **2020**, *739*, 137034.
[74] B. Hess, H. Bekker, H. J. C. Berendsen, J. G. E. M. Fraaije, *J. Comput. Chem.* **1997**, *18*, 1463–1472.
[75] A. Pérez, I. Marchán, D. Svozil, J. Sponer, T. E. Cheatham, C. A. Laughton, M. Orozco, *Biophys. J.* **2007**, *92*, 3817–3829.
[76] I. Ivani, P. D. Dans, A. Noy, A. Pérez, I. Faustino, A. Hospital, J. Walther, P. Andrio, R. Goñi, A. Balaceanu, G. Portella, F. Battistini, J. L. Gelpí, C. González, M. Vendruscolo, C. A. Laughton, S. A. Harris, D. A. Case, M. Orozco, *Nat. Methods* **2016**, *13*, 55–58.

[77] C. I. Bayly, P. Cieplak, W. Cornell, P. A. Kollman, *J. Phys. Chem.* **1993**, *97*, 10269–10280.
[78] F. Wang, J.-P. Becker, P. Cieplak, F.-Y. Dupradeau, *R. E. D. Python: Object oriented programming for Amber force fields*, Université de Picardie Jules Verne (France), Sanford Burnham Prebys Medical Discovery Institute, San Diego (USA) **2014**.
[79] E. Vanquelef, S. Simon, G. Marquant, E. Garcia, G. Klimerak, J. C. Delepine, P. Cieplak, F.-Y. Dupradeau, *Nucleic Acids Res.* **2011**, *39*, W511–W517.
[80] F.-Y. Dupradeau, A. Pigache, T. Zaffran, C. Savineau, R. Lelong, N. Grivel, D. Lelong, W. Rosanski, P. Cieplak, *Phys. Chem. Chem. Phys.* **2010**, *12*, 7821–39.
[81] U. Essmann, L. Perera, M. L. Berkowitz, T. Darden, H. Lee, L. G. Pedersen, *J. Chem. Phys.* **1995**, *103*, 8577–8593.
[82] E. F. Pettersen, T. D. Goddard, C. C. Huang, G. S. Couch, D. M. Greenblatt, E. C. Meng, T. E. Ferrin, *J. Comput. Chem.* **2004**, *25*, 1605–1612.
[83] F. Neese, F. Wennmohs, U. Becker, C. Riplinger, *J. Chem. Phys.* **2020**, *152*, 224108.
[84] A. D. Becke, *J. Chem. Phys.* **1993**, *98*, 5648–5652.
[85] J. P. Perdew, Y. Wang, *Phys. Rev. B* **1992**, *45*, 13244–13249.
[86] R. J. Gómez-Piñeiro, M. Drosou, S. Bertaina, C. Decroos, A. J. Simaan, D. A. Pantazis, M. Orio, *Inorg. Chem.* **2022**, *61*, 8022–8035.
[87] C. van Wüllen, *J. Chem. Phys.* **1998**, *109*, 392–399.
[88] E. van Lenthe, E. J. Baerends, J. G. Snijders, *J. Chem. Phys.* **1993**, *99*, 4597–4610.
[89] E. van Lenthe, E. J. Baerends, J. G. Snijders, *J. Chem. Phys.* **1994**, *101*, 9783–9792.
[90] F. Weigend, R. Ahlrichs, *Phys. Chem. Chem. Phys.* **2005**, *7*, 3297–3305.
[91] F. Neese, *Inorg. Chim. Acta* **2002**, *337*, 181–192.
[92] F. Neese, F. Wennmohs, A. Hansen, U. Becker, *Chem. Phys.* **2009**, *356*, 98–109.
[93] D. A. Pantazis, F. Neese, *Theor. Chem. Acc.* **2012**, *131*, 1292.
[94] G. Sciortino, G. Lubinu, J.-D. Maréchal, E. Garribba, *Magnetochemistry* **2018**, *4*, 55.

Manuscript received: August 3, 2023
Accepted manuscript online: August 21, 2023
Version of record online: October 24, 2023